TITLE PAGE

Structural basis of the negative allosteric modulation of 5-BDBD at human P2X4 receptors[✦]

Stefan Bidula[1], Izzuddin Bin Nadzirin[1], Marco M.D Cominetti[2], Harry Hickey[1], Sean A. Cullum[1], Mark Searcey[2], Ralf Schmid[3,4] and Samuel J. Fountain[1,5]

[1] School of Biological Sciences, University of East Anglia, Norwich Research Park, UK

[2] School of Pharmacy, University of East Anglia, Norwich Research Park, UK

[3] Leicester Institute of Structural and Chemical Biology, University of Leicester, UK

[4] Department of Molecular and Cell Biology, University of Leicester, UK

Abstract

The P2X4 receptor is a ligand-gated ion channel activated by extracellular ATP. P2X4 activity is associated with neuropathic pain, vasodilation and pulmonary secretion and therefore of therapeutic interest. The structure-activity relationship of P2X4 antagonists is poorly understood. Here we elucidate the structure-activity of 5-BDBD at human P2X4 by combining pharmacology, electrophysiology, molecular modelling and medicinal chemistry. 5-BDBD antagonised P2X4 in a non-competitive manner but lacked effect at human P2X2. Molecular modelling and site-directed mutagenesis suggested an allosteric binding site for 5-BDBD located between two subunits in the body region of P2X4, with M109, F178, Y300 and I312 on one subunit, and R301 on the neighbouring subunit as key residues involved in antagonist binding. The bromine group of 5-BDBD was redundant for the antagonist activity of 5-BDBD, though an interaction between the carbonyl group of 5-BDBD and R301 in P2X4 was significantly associated with 5-BDBD activity. 5-BDBD could inhibit the closed channel but poorly inhibited the channel in the open/desensitising state. We hypothesis that this is due to constriction of the allosteric site following transition from closed to open channel state. We propose that M109, F178, Y300, R301 and I312 are key residues for 5-BDBD binding, provide a structural explanation of how they contribute to 5-BDBD antagonism, and highlight that the limited action of 5-BDBD on open versus closed channels is due to a conformational change in the allosteric site.

Significance statement

Activity of P2X4 receptor is associated with neuropathic pain, inflammation and vasodilatation. Molecular information regarding small molecule interaction with P2X4 is very limited. Here we provide a structural explanation for the action of the small molecule antagonist 5-BDBD at the human P2X4 receptor.

Introduction

P2X receptors (P2X1-7) mediate the fast biological effects of extracellular ATP. They are a family of ligand-gated cation channels whose activation results in elevated cytoplasmic Ca^{2+} and membrane depolarisation. P2X receptors are attractive drug targets and recently clinically efficacious antagonists have been developed for some subtypes (Richards et al., 2019; Smith et al., 2020). P2X4 is a moderately desensitising ion channel (Fountain & North, 2006) that is activated by nanomolar extracellular ATP. Its activity has been implicated in flow-dependent vasodilation and remodelling of arteries (Yamamoto et al., 2006), cardiac contractility (Yang et al, 2014), production of inflammatory mediators (Layhadi et al., 2018), calcium signalling in human leukocytes (Layhadi & Fountain, 2019), surfactant secretion by type II alveolar epithelial cells (Miklavc et al., 2011) and neuropathic pain (Tsuda et al., 2003). As such, P2X4 is a promising therapeutic target with some recent advancement in selective antibody antagonists (Williams et al., 2019) and small molecule antagonists (Stokes et al., 2017; Illes et al., 2021) including PSB-12062 (Hernandez-Olmos et al., 2012), BX-430 (Ase et al., 2015), NP-1815-PX (Matsumura et al., 2016) and 5-BDBD (Fischer et al., 2004). Despite an increase in small molecules that antagonise P2X4, there remains limited information regarding the structure-activity relationship between antagonistic ligands and the P2X4 receptor. Information regarding the inhibitory mechanism of the benzodiazepine derivative 5-BDBD is contrasting and contradictory. Studies have suggested that 5-BDBD competes with ATP at the orthosteric binding site (Balazs et al., 2013; Coddou et al., 2019). In such studies, 5-BDBD causes a rightward shift in the ATP concentration-response curve with no reduction in the response maxima and with a potency similar to the competitive antagonist TNP-ATP (Balazs et al., 2013). In contradiction to these studies Abdelrahman et al (2017) demonstrate that TNP-ATP was capable of displacing [^{35}S] ATPγS from P2X4 but 5-BDBD could not, suggesting 5-BDBD has a negative allosteric, rather than competitive, mode of action. To this end, we have combined pharmacology, electrophysiology, *in silico* predictions, molecular dynamics and medicinal chemistry to understand the structure-activity relationship of 5-BDBD action at the human P2X4 receptor.

Materials and Methods

Cells and cell culture. The parental 1321N1 human astrocytoma cell line (RRID:CVCL_0110) and 1321N1 cells stably expressing either human P2X4 or human P2X2 receptors were maintained at 37°C and 5% CO_2 in DMEM (Lonza) supplemented with L-glutamine (4.1 mM), FBS (10% v/v; HyClone), penicillin/streptomycin (50 U/mL and 50 µg/mL, respectively; Gibco), and glucose (4.5 g/L). Cells were passaged twice weekly upon reaching 70-80% confluence and discarded upon reaching the 20th passage.

Drugs and basic salts. All basic salts and ATP were purchased from Sigma. 5-BDBD and BX-430 were purchased from Tocris Biosciences. 5-BDBD analogues with the following modifications were purchased from Vitas-M lab (R2-H, R3-Br; R2-H; R2-H, R3-CH₃; R2-H, R3-F; R1-Br, R2-H; R2-H, R1-Br; R2-H, R3-Cl; R1-Cl, R2-H).

Site-directed mutagenesis and transient transfection Human P2X4 cloned in pcDNA3.1 was mutated by PCR using the Q5 Site-Directed mutagenesis kit (New England Biolabs) and mutagenic primers designed using NEBaseChanger software (New England Biolabs). Cycling conditions for mutagenesis were as follows: Initial denaturation at 98°C for 30 seconds, followed by 25 cycles of 98°C for 10 seconds, 50-60°C for 20 seconds and 72°C for 5 minutes. A final extension was performed at 72°C for 2 minutes. Mutations were confirmed by sequencing and plasmid DNA was prepared using an ENZA Plasmid kit (Omega Bio-tek). For transient transfection of parental 1321N1 cells with pcDNA3.1 containing wild-type or mutated human P2X4 receptor, 1.25×10^4 cells/well were seeded in 96-well plates and cultured overnight at 37°C and 5% CO_2. Cells were transfected with a mixture of Lipofectamine 2000 (0.5 µL/well) and 300 ng/well plasmid DNA in Opti-MEM. Transiently transfected cells were used for experiments 72 hours after transfection.

Production of lentiviral particles and stable transfection. In brief, 9×10^6 HEK293/17 cells were incubated overnight in 150 mm culture dishes at 37°C and 5% CO_2. HEK293/17 were co-transfected with three plasmids; a lentiviral vector coding the viral genome with the transgene, psPAX2 containing a CAG promoter, and pMD2.G which encodes the Vesicular Stomatitis Virus envelope glycoprotein. The plasmids (24 µg DNA) and Lipofectamine 2000 were incubated together at room temperature for 20 min in Opti-MEM. The medium was replaced in the culture dishes with DMEM containing 1% (v/v) FBS and the plasmid mix was added in a drop-wise manner. Between day 2 and 4, the media was collected daily, passed through a 0.45 µm polyethersulfone filter (Whatman), and stored at 4°C. The virus was concentrated with Lenti-X Concentrator (Clontech Laboratories) at 4°C for 72 hours, then centrifuged at 1500 g for 45 minutes at 4°C. The supernatant was aspirated, pellet resuspended in DMEM, and suspension stored at -80°C. Viral titres were quantified using a QuickTiter™ Lentivirus Titer Kit (Cell Biolabs Inc) according to manufacturer's instructions. Absorbance was measured at 450 nm using a Flexstation 3 plate reader (Molecular Devices). To stably transfect 1321N1 astrocytoma cells, 2×10^5 cells were added to a 15 mL Falcon tube containing DMEM, polybrene (8 µg/mL; Sigma), and the viral media described above, prior to centrifugation at 1400 g for 1 h at 37°C. Cells exhibiting mCherry fluorescence were sorted using a BD FACSAria III Sorter (BD Biosciences) with excitation at 587 nm and emission at 610 nm.

Intracellular Ca^{2+} measurements. 1321N1 cells stably expressing human P2X2 or human P2X4 were seeded at 2.5×10^3 cells/well in poly-D-lysine-coated 96-well plates 24 hours prior to loading with Fura-2 AM calcium indicator dye (Abcam). 1321N1 transiently transfected with wild-type and mutant P2X4 receptors were loaded with Fura-2 AM 72 hours following transfection. Loading with Fura-2 AM was achieved by incubating cells for 1 hour at 37°C in loading solution containing 130 mM NaCl, 5 mM KCl, 8 mM D-glucose, 10 mM HEPES, 1.2 mM $MgCl_2$, 1.5 mM $CaCl_2$, 2 µM Fura-2 AM, and 0.01% (w/v) pluronic-F127; pH 7.4. Following loading, the buffer was replaced with salt buffered saline (loading solution without Fura-2 AM

and pluronic-F127). Cells were warmed for 10 minutes prior to calcium measurements. Fura-2 was measured at excitation wavelengths 340 nm and 380 nm with emission wavelength 520 nm using a Flexstation 3 plate reader. Sampling interval was 3.5 seconds with three reads/well. Fura-2 ratio was calculated using Softmax Pro v5.4, and responses were quantified using peak measurements.

Electrophysiology. Cells were resuspended at 1 x 10^6 cells mL in a solution containing 140 mM NaCl, 4 mM KCl, 1 mM MgCl$_2$, 2 mM CaCl$_2$, 5 mM D-glucose, and 10 mM HEPES; pH 7.4. Whole-cell patch clamp electrophysiology was performed using a Nanion Port-a-Patch system fitted with an eight-valve gravity-fed perfusion panel. Total solution exchange occurred in <150 ms. Internal solution contained 140 mM CsF, 10 mM NaCl, 2 mM EGTA, and 10 mM HEPES; PH 7.2. All recordings were performed in external solution containing 140 mM NaCl, 2 mM KCl, 2 mM CaCl$_2$, 1 mM MgCl$_2$, and HEPES; pH 7.4. In pre-incubation studies, 5-BDBD was perfused across the cells for 3 minutes prior to stimulation with ATP. In all other studies, ATP was perfused on to the cells for 2 secs, followed by immediate perfusion of ATP ± 5-BDBD, BX-430 or the DMSO vehicle control for 5 seconds. ATP, 5-BDBD and BX-430 were used at concentrations of 30 µM, 20 µM and 10 µM for all experiments, respectively. The DMSO vehicle control was at a final concentration of 0.1% (v/v). Acquisition protocols were run using HEKA PatchMaster software (RRID:SCR_000034). Data were sampled at 1 kHz and filtered at 10 kHz. Cells were held at -80 mV in all experiments and performed at room temperature (21-23°C). The values for τ were calculated by fitting a single exponential decay curve to the desensitisation phase of the current traces using OriginPro (v2019, Originlabs).

Homology modelling and ligand docking. 100 homology models for the human P2X4 receptor in the closed state were generated in Modeller 9v19 (Sali & Blundell, 1993) using the structure of the zebrafish P2X4 orthologue (62% pairwise sequence identity; PDB identifier: 4DW0) as a template following a standard protocol (Stavrou et al., 2020). The ten top-ranking models were prepared as a receptor ensemble for Rosetta ligand docking. 5-BDBD was prepared in
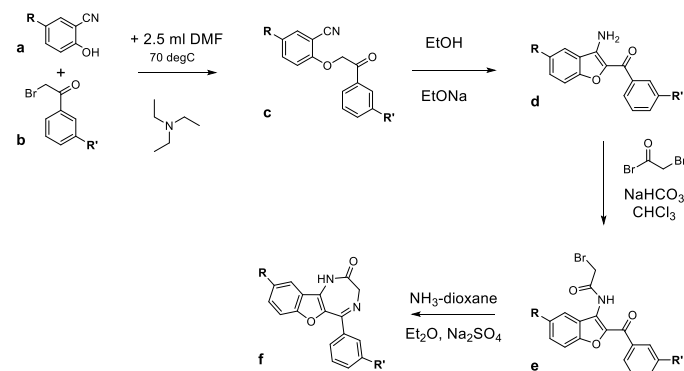
Marvin (v21.11; ChemAxon, https://www.chemaxon.com) and multiple conformers were generated using the frog2 server (Miteva et al., 2010). Following the docking strategy outlined in Lemmon & Meiler (2012) two series of Rosetta ligand docking (Davis & Baker, 2009) were run, sampling broadly the orthosteric site for ATP binding and a region equivalent to the previously identified allosteric binding site in P2X7 (Allsopp et al., 2017) generating 10,000 docking poses for each combination of site and ensemble structure. From each site the 1,000 docked complexes with the lowest total Rosetta energy were clustered (Roe & Cheatham, 2013) to identify groups of alternative binding modes. Representative poses with the lowest Rosetta interface delta scores from the largest cluster and best scoring poses were visualized in PyMol and served as starting structures for molecular dynamics simulations for further analysis. The 5-BDBD analogue 3D models were generated using CACTVS (National Cancer Institute) and were prepared for docking using LigPrep software (www.schrodinger.com). Induced fit docking of the allosteric site on the homology model above was performed using the automated extended sampling protocol within the Schrödinger Maestro suite (www.schrodinger.com) using an OPLS3e force field. The top 1,000 docking poses were retained from 10,000 docking poses. Structures within 30 kcal mol^{-1} of the lowest energy structure were retained and representative docks were visualised using Chimera.

Molecular dynamics. Molecular dynamics simulations were run in AMBER18 using the ff14SB and GAFF force fields (Case et al., 2018). 5-BDBD parameters were generated in antechamber using AM1-BCC charges. The extracellular domain of the P2X4 receptor models including docked 5-BDBD was surrounded with a cubic 12 Å TIP3P water box and charge neutralised at 0.15M Na$^+$ and Cl$^-$ (Machado & Pantano, 2020). System equilibration started with three rounds of steepest descent energy minimisation followed by conjugate gradient minimisation with restraints on non-hydrogen atoms in the first round, restraints on non-solvent molecules in the second round and no restraints in round three. The system was then heated at constant volume from 0-300 K within 50 ps with position restraints on protein and ligand (2.0 kcal mol^{-1} Å^{-2}). This was followed by a 100 ps equilibration step and 500 ns production

runs. All simulations steps used periodic boundary conditions, the SHAKE algorithm for bonds involving hydrogens, a Langevin thermostat for temperature control, and a Monte Carlo barostat for the equilibration step and production runs. Replicates for the allosteric site simulations were set up by placing 5-BDBD in symmetrically equivalent positions between different subunits. Trajectories and ligand binding were analysed in cpptraj (Roe & Cheatham, 2013).

General chemistry. All reagents and solvents were purchased from Merck, Fisher Scientific and Fluorochem and used as received. NMR solvents were purchased from Goss Scientific. NMR data was recorded with a Bruker instrument operating at the specified frequency and with the described solvent. Shifts are recorded in ppm and referenced to the solvent residual peak. High resolution mass spectrometry was provided by the EPSRC NMSF facility at Swansea. Melting points were recorded on a Stuart Scientific Melting Point Apparatus SMP3.

Chemical synthesis of 5-BDBD analogues. All chemical analogues were synthesised using the general scheme below:

Synthesis of the compounds follows a reported procedure (Fischer et al., 2004) with minor modifications. Intermediate purification is not necessary and was only performed for the final product. A mixture of 5-substituted-2-hydroxybenzonitrile (a, 250 mg, 1 eq), 3-substituted-phenacyl bromide (b, 1 eq) and triethylamine (1.1 eq) in 2.5 mL of dimethylformamide was stirred at 70 °C until completion (2-6 hours) was confirmed by TLC. The reaction mixture was cooled down to room temperature, diluted with 100 mL of ethyl acetate and washed with water (3 x 30mL) and brine (1 x 30 mL). The organic layer was dried over sodium sulfate and evaporated under reduced pressure. The residue (crude c) was dissolved in 10 mL of ethanol and 1.1 equivalents of sodium ethoxide were added thereto. The mixture was stirred at 80 °C in a sealed tube for 2-12 hours, until completion was confirmed by TLC. The reaction mixture was cooled down to room temperature, diluted with 100 mL of ethyl acetate and washed with water (3 x 30 mL) and brine (1 x 30mL). The organic layer was dried over sodium sulfate and evaporated under reduced pressure. A stirring mixture of the residue (crude d) and sodium hydrogen carbonate (4 eq) in 30 mL of chloroform was cooled down to 0 °C. Bromoacetyl bromide (1.1 eq) was slowly added thereto and the mixture was then stirred for 1-2 hours, until completion was confirmed by TLC. The mixture was diluted with 100 mL of ethyl acetate, washed with a saturated solution of sodium hydrogen carbonate (1 x 30 mL) and with brine (1 x 30 mL). The organic layer was dried over sodium sulfate and evaporated under reduced pressure. A mixture of the residue (crude e), 7 mL of diethyl ether, NH_3-Dioxane 0.5 M (10 eq) and 1.5 g of anhydrous sodium sulfate were stirred in a sealed tube for 3 days. The mixture was diluted with 100 mL of ethyl acetate, washed with water (3 x 50 mL) and with brine (1 x 50 mL). The organic layer was dried over sodium sulfate and evaporated under reduced pressure. The product was purified by flash chromatography and then triturated with diethyl ether to give the pure product (f). Where necessary, an additional purification by preparative HPLC was performed. Purity and characterization were assessed according to the attached methods. Supporting information regarding synthesised compounds including high-resolution mass spectrometry (HRMS) and nuclear magnetic resonance spectroscopy (NMR) is given in **Supplemental data.**

Flash chromatography. All silica employed was Davisil® Silica 60A, particle size 40-63 micron, purchased from Fisher Scientific. Dichloromethane (solvent A) and methanol (solvent B) were purchased either from Fisher Scientific or Merck. 10 g SNAP columns purchased from Biotage were refilled with the silica described above using vacuum packing. Crude samples were adsorbed on 1 g of silica and loaded on a pre-equilibrated column. The sample was eluted with 1 column volume (CV) of A, a linear gradient to 10 % B over 10 CVs and then the concentration was maintained constant for 2 CVs. Collection parameters were set to monitor at 254 and 280 nm, with a collection threshold of 30 mAU.

Preparative HPLC. All preparative HPLC work was performed on an Agilent Technologies 1200 Infinity series equipped with an Agilent Eclipse XDB-C18, 5µM, 21.2 × 150mm. Samples were detected by UV absorbance at 210nm. All solvents were HPLC grade and purchased either from Merck or Fisher Scientific. The samples were eluted with water/acetonitrile 95/5 + 0.05% trifluoroacetic acid (solvent **A**) and acetonitrile/water 95/5 + 0.05% trifluoroacetic acid (solvent **B**) using the gradient method reported below. It is important to note that some samples produce split peaks in the presence of TFA, likely due to the equilibrium between the open and closed form of the diazepinone ring; removing the acid from solutions A and B prevents the issue. The samples were dissolved in solvent **B** and filtered on 0.45 µM PTFE filters before injection. The fractions containing the product were collected and the acetonitrile was removed by evaporation under reduced pressure. The remaining water was freeze dried to yield the dry product. Gradient: 100% **A** until minute 3, then linear gradient to 100 % **B** in 7 minutes, followed by 5 minutes at 100 % **B**. In 5 minutes the eluent is brought back to 100 % **A** before the following analysis.

Analytical HPLC. All analytical HPLC measurement were performed on an Agilent Technologies 1200 series equipped with an Agilent Eclipse XDB-C18, 5µM, 4.6 × 150mm. Samples were detected by UV absorbance at 210nm. The column compartment was maintained at 40 °C. All solvents were HPLC grade and purchased either from Merck or Fisher Scientific. The samples were eluted with water + 0.05% trifluoroacetic acid (solvent **A**) and acetonitrile + 0.05% trifluoroacetic acid (solvent **B**) using the gradients in the methods below. The samples were dissolved in solvent **B** and filtered on 0.45 µM PTFE filters before injection. Solvent **B** was also used as a blank. Data analysis was performed with OpenLAB CDS ChemStation Edition by Agilent Technologies. Purity was determined by peak integration. The blank was subtracted from the signal of the sample prior to integration. It is important to note that some samples produce split peaks in the presence of TFA, likely due to the equilibrium between the open and closed form of the diazepinone ring; removing the acid from solutions A and B prevents the issue. This will be specified with the data reported for each compound. Method 1: 100 % **A** until minute 3, then linear gradient to 95 % **B** in 7 minutes, followed by 5 minutes at 95 % **B**. In 5 minutes the eluent is brought back to 100 % **A** before the following analysis. Method 2: 100 % **A** until minute 2, then linear gradient to 95 % **B** in 3 minutes, followed by 5 minutes at 95 % **B**. In 5 minutes the eluent is brought back to 100 % **A** before the following analysis.

Experimental design & statistical analysis. Experimental design, analysis and disclosure follows the guidance outlined by Curtis et al., (2018). Studies were designed to groups of equal size using randomisation and blinded analysis where technically or practically feasible. Data are expressed as mean $\pm$ SEM, and n is the number of technical repeats. Statistical analysis was performed using independent values from technical or biological repeats. Statistical analysis was only performed on dataset where n$\geq$5 using OriginPro software (v2019; OriginLab). A threshold for statistical analysis of $p<0.05$ was applied throughout. Data were first tested with a Shapiro–Wilk test for normality and Levene's test for equality of variance. Population means were compared with an ANOVA for parametric datasets and Mann-Whitney test for non-parametric datasets if F in ANOVA achieved the necessary level of statistical

significance. Data outliers were included in all analysis and presentation of data. Data normalisation to control values has been applied to control for inter-experimental variation where applicable. For transformed dataset (e.g. data expressed as % control), test data points are normalised to control values within the same technical repeat.

For antagonist IC_{50} data sets, the normalised response was plotted against Log10 antagonist concentration and fitted with a modified Hill equation as below:

$$Y = Start + (End - Start)\frac{X^n}{k^n + X^n}$$

where k = Michaelis constant and n = number of cooperative sites. The data sets were then compared with an F test.

Pairwise comparison of EC_{50} and IC_{50} values generated in curve shift experiments was conducted using a paired sample t test. Tau (τ) was estimated by fitting a single exponential decay curve to the desensitisation phase of current traces:

$$Y = A \times \exp\left(\frac{-x}{t}\right) + Y0$$

where Y0 = offset, A = amplitude, and t = time constant.

Nomenclature of targets and ligands   Key protein targets and ligands in this article are hyperlinked to corresponding entries in **http://www.guidetopharmacology.org**, the common portal for data from the IUPHAR/BPS Guide to PHARMACOLOGY (Harding et al., 2018), and are permanently archived in the Concise Guide to PHARMACOLOGY 2017/18 (Alexander et al., 2017).

Results

5-BDBD activity at human P2X4, human P2X2 and chimeric receptors

ATP could evoke concentration-dependent intracellular Ca^{2+} responses in 1321N1 astrocytoma cells stably expressing either human P2X4 or human P2X2 receptors (**Figure 1a**) with EC_{50} values 458 ± 42 nM (N=6) and 891 ± 56 nM (N=6), respectively. ATP-evoked responses were not observed in untransfected cells. 5-BDBD antagonised human P2X4 with an IC_{50} 780 ± 24 nM (N=8) (**Figure 1b**) but had no significant effect on human P2X2 across the concentration range tested (**Figure 1b**). 5-BDBD caused a significant decrease in the human P2X4 response maxima ($p<0.05$; N=6) and small but significant increases in ATP EC_{50} (control $vs \geq 10$ μM 5-BDBD; $p<0.05$; N=6), indicating a negative allosteric mechanism of action (**Figure 1c**). Next, we took advantage of the human P2X2 receptor insensitivity to 5-BDBD to make a series of receptor chimeras, substituting sequential 10 amino acid sections in the ectodomain of the human P2X4 receptor with the equivalent residues of P2X2. The majority of chimeras were functional and mediated ATP-evoked Ca^{2+} responses when expressed in 1321N1, with the exception of substitutions at amino acid positions 71-80, 101-110, 131-140, 201-210, 221-220, 261-270, 281-290 and 291-300, which were non-responsive to ATP (≤100 μM; N=5). 5-BDBD sensitivity was retained in all P2X4-P2X2 chimeric receptors (N=5; $p>0.05$) except for the chimera baring substitutions at amino acid positions 81-90 (N=5; $p<0.05$) (**Figure 1d**). These amino acids were located towards the top of the body region of the receptor and extended towards the orthosteric site for ATP binding (**Figure 1e**).

In silico identification and interrogation of an allosteric binding site for 5-BDBD

To explore putative binding poses of 5-BDBD to the P2X4 receptor, the orthosteric ATP binding site and a pocket equivalent to the allosteric site identified in P2X7 (Bin Dayel et al., 2019) were sampled using Rosetta ligand docking. Docking was performed using a homology model of human P2X4 in the closed conformation. Comparing the top docking scores for both sites clearly pointed towards an allosteric binding mode with best scores of -17.5 and -15.0 for allosteric and orthosteric poses, respectively. In the predicted allosteric binding pose 5-BDBD sat between two P2X4 subunits with residues of three beta strands from the beta sheet located in the "body" of the first P2X4 subunit (V105, L107, M109; F296, K298, Y300; T310, I312) forming one side of the cavity (**Figure 2a, Supplemental Figure 1**). The other side of the cavity comprised three regions with F178 and L179 adjacent to the aforementioned beta sheet, residues L79, R82, W84 and D88 forming a second region, and contributions from residues W164, Y299, R301 and E307 of the second subunit (**Figure 2a**). While the highest ranked predicted allosteric docking poses of the largest cluster shared common features, there were also differences. For instance, it was not conclusive how much R301 and R82 were involved in hydrogen bonding to the 5-BDBD carbonyl group or whether E307 or Y300 might be involved in coordinating the 5-BDBD amide-NH.

Predicted binding modes identified via Rosetta ligand docking were further explored by four 500 ns MD simulations of the extracellular domain of the human P2X4 receptor. The three simulations for the allosteric binding mode and the control simulation for an orthosteric binding mode remained stable in all simulations with Cα-rmsd values of less than 3.5 Å (**Supplemental Figure 2 a-d**). In the simulation of the orthosteric mode the ligand did not remain in its starting position but moved ≈7 Å out of the orthosteric site (**Supplemental Figure 2 h**), supporting the notion that orthosteric binding was less favourable. For the MD simulations with 5-BDBD located in the allosteric binding site, such movement out of the binding pocket was not observed (**Supplemental Figure 2 e-g)**, and these simulations were further analysed

for the presence of specific interactions. While not fully conclusive, the simulations favoured R301 over R82 as an interaction partner for the 5-BDBD carbonyl with the guanidinium-carbonyl interaction forming stably in two replicates (**Figure 2b**). From ligand docking, the 5-BDBD amide-NH could potentially interact with Y300 or E307. In all three replicates the distance between E307 and 5-BDBD NH quickly increased to values unfavourable for hydrogen bonding (**Figure 2c**). For Y300, the hydroxyl group moved at least partially into a position where a hydrogen bond to 5-BDBD-NH was feasible (**Figure 2d**). Calculating hydrophobic contacts between 5-BDBD and the receptor suggested contributions from L79, W84, V105, L107, M109, F178, Y299 and I312 to antagonist binding (**Figure 2e**). From the analysis of the molecular dynamics simulations a picture emerged where R301 and Y300 from different subunits were predicted to be key residues for coordinating the carbonyl and amide group, and a series of hydrophobic residues in the binding pocket were contributing to 5-BDBD binding.

Interrogation of the 5-BDBD binding pose by receptor mutagenesis and medicinal chemistry

We further tested the fidelity of the *in silico* docking pose by generating a series of point mutations in human P2X4, substituting single residues for their equivalent in human P2X2 (**Figure 3a**). Docking and MD simulations suggested that W84, L107, M109, F178 and I312 might contribute favourably to 5-BDBD binding. We investigated the key residues predicted to interact with 5-BDBD and those that form the hydrophobic lining of the pocket. W84A, D88A, L107A, G305T and E307T substitutions had no effect of the activity of 5-BDBD (*N*=5, *p*>0.05; **Figure 3b**). In support of MD stimulations, R301K but not E307T substitution caused a significant loss of 5-BDBD activity (*N*=5, *p*<0.05; **Figure 3b**). Modelling of the R301K mutation suggested that the shorter chain length of lysine (K) versus arginine (R) creates a distance unfavourable (> 5Å) for hydrogen bond formation between the amine-carbonyl groups of the residue and ligand (**Figure 3c and 3d**). In addition, R82K or R82A substitutions had no effect

on 5-BDBD activity (N=6, p>0.05; **Figure 3b**). These data are in agreement with MD simulations which favour R301 over R82 in interacting with 5-BDBD (**Figure 2c**). Loss of 5-BDBD activity at the Y300A mutant receptor (N=5, p<0.05; **Figure 3b**) supported a role for Y300 in 5-BDBD interactions (**Figure 2c**), and the unfavourability of E307 identified in MD stimulations was supported by intact 5-BDBD activity at the E307T mutant (N=5, p>0.05; **Figure 3c**).

Hydrophobicity of residue 107 is conserved in human P2X2 (**Figure 3a**), consequently the L107A mutation conserved 5-BDBD activity (**Figure 3b**). However, hydrophobicity is not conserved at residues 81 and 109 in P2X2 (N=5, p>0.05; **Figure 3a**) and mutation to the basic residue histidine equivalent to these positions in P2X2 resulted in a significant reduction in 5-BDBD activity (N=5, p<0.05; **Figure 3b**). Mutation of F178 to L178, which is in close proximity to the 5-BDBD Br-phenyl moiety in the preferred docking pose, was not tolerated and resulted in loss of 5-BDBD activity (N=5, p<0.05; **Figure 3b**). Finally, when I312 was mutated, which showed a fairly consistent interaction with the 5-BDBD benzofurane moiety, the activity of 5-BDBD was significantly reduced (N=5, p<0.05; **Figure 3b**). While there was some loss of 5-BDBD activity in the W84A mutant, the MD and modelling predicted a more significant loss and this result was unexpected (**Figure 3b**). Agreement between modelling and experimental data supported the role of F178, Y300, R301 and I312G as four key anchoring points for the 5-BDBD ligand, in addition to M109 in the hydrophobic lining of the binding pocket.

To further probe the proposed binding pocket, we generated or purchased several analogues of 5-BDBD that would allow the ligand chemical space in relation to the pocket to be explored. The 5-BDBD analogues had modifications at position R1, R2 and R3 (**Figure 4a**). Halogen substitutions (Cl and F) of Br at position R2 were well tolerated with no significant change in activity and with similar predicted docking poses to 5-BDBD (N=5; **Figure 4b, c; Supplemental Figure 3**), though substitution with a bulkier trifluoromethyl (CF_3) group caused a significant reduction in activity (N=5; **Figure 4b, c**). Interestingly, substitution of Br with H

led to a retention in antagonist potency and slight enhancement of inhibitory activity (N=5; **Figure 4b, c**), revealing the dispensability of Br at position R2. Strikingly, movement to Br from R2 to R3 was not tolerated, leading to complete loss of antagonist activity (N=6; **Figure 4b, c**). Likewise, substitutions of other chemical groups at position R3 were also not tolerated (**Figure 4b, c**). Docking analysis of ligands with R3 substitutions revealed an inability to fully enter the pocket. This was likely due to the Y300 and R301 side chains anchoring the amide of 5-BDBD which would lead to a steric clash between the beta-sheet in region A72-W84 and R3 when replacing the H with larger substitutions (**Supplemental Figure 4**). For R2, docking and molecular dynamics simulations predicted that the Br either pointed towards the solvent, or by rotation of the phenyl ring into the hydrophobic binding pocket. For both scenarios, chemically similar substitutions are likely to be tolerated. Docking predicted that the R1 position pointed deeper towards the hydrophobic pocket lining and thus we tested the effect of new chemical groups at this position by paired substitutions at R1 and R2 positions. In these experiments, substitution of H with Br at R1 caused complete loss of antagonist activity (N=5; **Figure 4b, c**). Complete loss of activity was also observed for the R1:R2 F and R1:R2 CF_3 substitutions (**Figure 4b, c**), though the R1:R2 Cl substitution was tolerated and resulted in slightly enhanced antagonist activity (N=5; **Figure 4b, c**). Docking analysis revealed a similar pose for R1:R2 Cl as 5-BDBD (**Supplemental Figure 5**), though other R1:R2 substituents were unable to penetrate into the binding site (**Supplemental Figure 5**). As the R2 Br was not required for 5-BDBD we further investigated R1 substitutions in the absence of R2 Br. Surprisingly, now R1 substitutions were fairly well tolerated with zero or modest changes in antagonist activity (**Figure 4b, c**). Docking of these ligands revealed an almost mirror-image of the docking pose observed for 5-BDBD and R2 analogues, with the R1 group now protruding from the binding site and R2 position facing into the pocket (**Supplemental Figure 6**). Further *in silico* measurement of the docking poses were made to fully understand the effect of chemical substitution on antagonist activity. Quantification of the distance between the carbonyl group of 5-BDBD and analogues and R301 indicated a correlation between distance and antagonist activity (**Figure 4d**). Analysis revealed that if the carbonyl group of 5-

BDBD analogues were within 4 Å of the guanidinium group of R301 then antagonist activity was retained, though distances > 8 Å resulted in loss of activity (**Figure 4d**). The activity of 5-BDBD was also related to the depth of ligand penetration into the binding pocket (**Figure 4e**).

Receptor state-dependency of 5-BDBD activity is associated with conformational changes in the binding pocket

Analysis of the identified binding pocket in homology models of the P2X4 receptor in the closed versus the open state revealed a conformational change (**Figure 5a**) that could possibly result in a state-dependent action of 5-BDBD. *In silico* measurement of the residues lining the entrance to the pocket revealed a constriction of the opening relative to L107 when the channel moved from a closed to open state (**Figure 5b; Supplemental Table 1**). Consistently, docking analysis failed to dock 5-BDBD within the allosteric binding pocket of the open channel. This analysis predicted an ability of 5-BDBD to bind better and effectively antagonise human P2X4 in the closed state but have more limited activity in the open channel conformation. To test this hypothesis, we compared the ability of 5-BDBD to block human P2X4 currents following pre-incubation with 5-BDBD (incubation with closed state) compared to application of 5-BDBD when the channel was bound with ATP. This was achieved using whole-cell patch clamp electrophysiology and rapid solution switching. In these experiments, incubation with 5-BDBD prior to ATP challenge effectively inhibited channel activity (**Figure 5c**), though 5-BDBD exhibited very limited activity when co-applied with ATP (**Figure 5d**). In contrast, BX-430, which is predicted to share some common residues for binding with those identified in this study (Ase et al., 2019), efficiently antagonised P2X4 upon co-application with ATP (**Figure 5e**). The differences between 5-BDBD and BX-430 were apparent when comparing the their current decay constants in response to antagonist application (**Figure 5f**).

Discussion

The complementary approaches of molecular modelling, receptor mutagenesis and ligand medicinal chemistry supported a negative allosteric action of 5-BDBD by binding to an inter-subunit pocket located in the body region of human P2X4. We propose that M109, F178, Y300, R301 and I312 are key anchor points for 5-BDBD binding, provide a structural explanation of how they contribute to 5-BDBD antagonism, and highlight that the limited action of 5-BDBD on open versus closed channels is due to a conformational change in the proposed binding pocket.

The current mechanism of action for 5-BDBD remains controversial. Initial studies demonstrated that 5-BDBD competed with ATP for the orthosteric site (Balazs et al., 2013; Coddou et al., 2019). Conversely, recent studies by Abdelrahman *et al.,* (2017) used a radioactively labelled derivative of the ATP analogue ATPγS ([^{35}S]ATPγS) to dispute the competitive nature of 5-BDBD. The authors found that TNP-ATP could displace [^{35}S]ATPγS, but neither 5-BDBD or the allosteric antagonist paroxetine competed with [^{35}S]ATPγS for the orthosteric site. Our data agree with the latter observations and there is growing evidence to support an allosteric mode of action for other P2X4 antagonists including PSB-12054, PSB-12062 and BX-430 (Hernandez-Olmos et al., 2012; Ase et al., 2015). In-depth analysis of the predicted allosteric site identified several potentially interacting residues on the α-helices and β-subunits of P2X4 including F178 (α2), R82, W84 (β3), V105, L107, M109 (β4), Y300 (β13) and I312 (β14) on one subunit and R301 (β13), G305 and E307 (β14) on the neighbouring subunit. Site-directed mutagenesis identified that M109, F178, Y300, I312 and R301 as residues contributing most to 5-BDBD activity, whilst W84, L107, and G305 were only marginally implicated. Indeed, Y300 and I312 were found to be critical for the inhibitory activity of BX-430 towards P2X4 (Ase et al., 2019). Although 5-BDBD and BX-430 are chemically distinct (albeit both contain bromines), it is feasible that both could bind to a similar site in P2X4 given the chemical promiscuity of the equivalent site in P2X7. Interestingly, I312 may be intrinsically linked with channel opening in P2X4, as mutation of this residue to leucine and

glycine could disrupt BX-430 inhibition, whilst mutation to tyrosine and tryptophan could convert BX-430 into a positive allosteric modulator (Ase et al., 2019).

The R301 residue in P2X4 was found to be significantly implicated in 5-BDBD activity. Here, the guanidinium group was predicted to form hydrogen bonds with the carbonyl on the diazepinone ring of 5-BDBD. When R301 was mutated to lysine, which shares similar chemical properties, *in silico* predictions suggested that the R301K mutation increased the interaction distance between the lysine and the carbonyl group. Further *In silico* modelling of 5-BDBD analogues reinforced the link between R301 to carbonyl distance and inhibitory activity. It is also noteworthy that R301 (with the exception of P2X5) is not conserved in other human P2X receptor subtypes. These findings could contribute to the generation of more potent and selective antagonists.

To date, R301 has not previously been directly implicated in the activity of antagonists at P2X4. However, previous studies in P2X7 showed that mutating the D92 residue could destabilise the β-sheet containing Y291-E301. This indirectly reduced the participation of K300 (equivalent to R301 in P2X4) in the binding pocket from 85% to 23%, and antagonist activity was subsequently weakened. Notably, in P2X7, the movements of β13 and β14 strands in the upper body domain also seem to be tightly coupled to channel opening (Karasawa and Kawate, 2016). It is plausible that this is also likely for P2X4, and interactions between 5-BDBD with R301 and I312 on the β13 and β14 strands, respectively, may stabilise the closed conformation and inhibit the necessary movements of these β-strands to initiate channel opening upon ATP binding (Karasawa and Kawate, 2016). Furthermore, it could also be hypothesised that mutation of F81 may limit 5-BDBD binding in a similar manner to D92 in P2X7. In the predicted binding pose, F81 is located on the periphery of the β3-strand and is not within proximity of 5-BDBD in the proposed binding site. Therefore, it is unlikely that F81 directly interacts with 5-BDBD, but instead induces a conformational change along the β3-sheet, affecting the involvement of potentially interacting residues lining the pocket. Mutation

of P2X7 residues 81-94 (77-86 in P2X4) and 112-118 (109-115 in P2X4) prevented inhibition of P2X7 by AZ10606120 (Allsopp et al., 2017). This region has since been implicated in the activity of numerous chemically distinct antagonists of P2X7, including A438079, A740003, A804598, GW791343, JNJ47965567, AZ11645373, Brilliant Blue G, KN-62, calmidazolium and ZINC58368839 (Bin Dayel, 2019).

We had initially hypothesised that the bromine would be critical to the inhibitory activity of 5-BDBD. However, substitution of the bromine with other halogens at position R2 or moving the bromine to position R1 was tolerable and did not significantly alter the activity of 5-BDBD. Moreover, the redundancy of the halogen was verified when an analogue lacking halogen's had greater inhibitory capacity. All these analogues could likely form stable hydrogen bonds with R301, which we hypothesised to be a critical interaction for 5-BDBD inhibition. Conversely, halogen substitutions to R3 were not tolerated. As aforementioned, this was most likely due to a steric clash with residues lining the binding pocket, preventing the molecule from entering the site.

To support our pharmacological observations, whole-cell patch-clamp electrophysiological readings were conducted. We found that pre-treatment with 5-BDBD was able to significantly inhibit P2X4 channel opening, but application of 5-BDBD to desensitising P2X4 could poorly inhibit. Investigations into the respective allosteric site in P2X7 (Karasawa & Kawate, 2016) showed that the allosteric cavity shrinks upon receptor activation; allowing the lower body region to widen for full channel opening. Indeed, comparisons between the homology models of P2X4 in the open and closed state highlighted that the allosteric site in P2X4 in the open state was also smaller and less accessible. In the open state, the β3 (containing T76, S77, L79, R82, and W84) and β4 sheets (containing L107) came much closer together and the residues lining these β sheets appeared to occupy and occlude the binding site. Therefore, upon channel opening, it's plausible that the entry of 5-BDBD to this site is limited, resulting in a weakened/delayed ability to inhibit P2X4. During the desensitisation phase the conformation

of P2X4 begins to relax, potentially increasing the availability of the binding pocket. Given that 5-BDBD and BX-430 are a similar molecular weight and occupy a similar volume, why BX-430 can inhibit the desensitising channel much faster than 5-BDBD is unknown. Regarding the chemical properties of 5-BDBD and BX-430, 5-BDBD has one rotatable bond, whereas BX-430 has three. In general, molecules with fewer rotatable bonds are preferable as ligands because they have a smaller conformational entropy change upon binding (Gao et al., 2010). However, in this particular case it could be possible that the enhanced molecular flexibility of BX-430 allows it to adapt to the conformational changes of P2X4 during desensitisation and adopt the orientation necessary for binding much quicker than 5-BDBD.

Taken together, we show that 5-BDBD acts as a negative allosteric modulator of human P2X4 by making inter-subunit interactions in the body region. The observations made here provide key insights into the comparable but contrasting activities of 5-BDBD and BX-430 towards human P2X4. Furthermore, this study enhances our understanding of the structural interactions underlying P2X4 inhibition and provides critical information to aid in the development of novel, more potent antagonists to treat P2X4-driven pathologies (Braganca & Correia-de-Sa, 2020).

Acknowledgments

Author contributions

Participated in research design: Fountain, Bidula, Searcey and Schmid

Conducted experiments: Bidula, Bin Nadzirin, Cominetti, Hickey and Cullum

Performed data analysis: Bidula, Bin Nadzirin, Cominetti, Hickey, Cullum and Schmid

Wrote or contributed to the writing of the manuscript: Fountain, Schmid, Bidula and Cominetti

The authors declare that they have no conflicts of interest with the contents of this article.

References

Abdelrahman A, Namasivayam V, Hinz S, Schiedel AC, Kose M, Burton M, et al. (2017). Characterization of P2X4 receptor agonists and antagonists by calcium influx and radioligand binding studies. Biochem Pharmacol 125: 41-54.

Alexander SP, Kelly E, Marrion NV, Peters JA, Faccenda E, Harding SD, et al. (2017). THE CONCISE GUIDE TO PHARMACOLOGY 2017/18: Overview. Br J Pharmacol 174 Suppl 1: S1-S16.

Allsopp RC, Dayl S, Schmid R, & Evans RJ (2017). Unique residues in the ATP gated human P2X7 receptor define a novel allosteric binding pocket for the selective antagonist AZ10606120. Sci Rep 7: 725.

Ase AR, Honson NS, Zaghdane H, Pfeifer TA, & Seguela P (2015). Identification and characterization of a selective allosteric antagonist of human P2X4 receptor channels. Mol Pharmacol 87: 606-616.

Ase AR, Therrien E, & Seguela P (2019). An Allosteric Inhibitory Site Conserved in the Ectodomain of P2X Receptor Channels. Front Cell Neurosci 13: 121.

Balazs B, Danko T, Kovacs G, Koles L, Hediger MA, & Zsembery A (2013). Investigation of the inhibitory effects of the benzodiazepine derivative, 5-BDBD on P2X4 purinergic receptors by two complementary methods. Cell Physiol Biochem 32: 11-24.

Bin Dayel A, Evans RJ, & Schmid R (2019). Mapping the Site of Action of Human P2X7 Receptor Antagonists AZ11645373, Brilliant Blue G, KN-62, Calmidazolium, and ZINC58368839 to the Intersubunit Allosteric Pocket. Mol Pharmacol 96: 355-363.

Braganca B, & Correia-de-Sa P (2020). Resolving the Ionotropic P2X4 Receptor Mystery Points Towards a New Therapeutic Target for Cardiovascular Diseases. Int J Mol Sci 21.

Case DA, Ben-Shalom IY, Brozell SR, Cerutti DS, Cheatham TE, Cruzeiro VWD et al (2018). AMBER 2018, University of California, San Francisco.

Curtis MJ, Alexander S, Cirino G, Docherty JR, George CH, Giembycz MA, Hoyer D, Insel PA, Izzo AA, Ji Y, MacEwan DJ, Sobey CG, Stanford SC, Teixeira MM, Wonnacott S, Ahuwalia A (2018). Experimental design and analysis and their reporting II: updated and simplified guidance for authors and peer reviewers. Br J Pharmacol 175: 987-993.

Coddou C, Sandoval R, Hevia MJ, & Stojilkovic SS (2019). Characterization of the antagonist actions of 5-BDBD at the rat P2X4 receptor. Neurosci Lett 690: 219-224.

Davis IW, & Baker D (2009). RosettaLigand docking with full ligand and receptor flexibility. J Mol Biol 385: 381-392.

Fischer R, Kalthof B, Gruetzmann, R, Woltering E, Stelte-Ludwig B, & Wuttke (2004). Benzofuro-1,4-diazepin-2-one derivatives. Patent CA2519987A1.

Fountain SJ, & North RA (2006). A C-terminal lysine that controls human P2X4 receptor desensitization. J Biol Chem 281: 15044-15049.

Gao C, Park MS, & Stern HA (2010). Accounting for ligand conformational restriction in calculations of protein-ligand binding affinities. Biophys J 98: 901-910.

Harding SD, Sharman JL, Faccenda E, Southan C, Pawson AJ, Ireland S, et al. (2018). The IUPHAR/BPS Guide to PHARMACOLOGY in 2018: updates and expansion to encompass the new guide to IMMUNOPHARMACOLOGY. Nucleic Acids Res 46: D1091-D1106.

Hernandez-Olmos V, Abdelrahman A, El-Tayeb A, Freudendahl D, Weinhausen S, & Muller CE (2012). N-substituted phenoxazine and acridone derivatives: structure-activity relationships of potent P2X4 receptor antagonists. J Med Chem 55: 9576-9588.

Illes P, Muller CE, Jacobson KA, Grutter T, Nicke A, Fountain SJ, et al. (2021). Update of P2X receptor properties and their pharmacology: IUPHAR Review 30. Br J Pharmacol 178: 489-514.

Karasawa A, & Kawate T (2016). Structural basis for subtype-specific inhibition of the P2X7 receptor. Elife 5.

Layhadi JA, & Fountain SJ (2019). ATP-Evoked Intracellular Ca(2+) Responses in M-CSF Differentiated Human Monocyte-Derived Macrophage are Mediated by P2X4 and P2Y11 Receptor Activation. Int J Mol Sci 20.

Layhadi JA, Turner J, Crossman D, & Fountain SJ (2018). ATP Evokes Ca(2+) Responses and CXCL5 Secretion via P2X4 Receptor Activation in Human Monocyte-Derived Macrophages. J Immunol 200: 1159-1168.

Lemmon G, & Meiler J (2012). Rosetta Ligand docking with flexible XML protocols. Methods Mol Biol 819: 143-155.

Machado MR, & Pantano S (2020). Split the Charge Difference in Two! A Rule of Thumb for Adding Proper Amounts of Ions in MD Simulations. J Chem Theory Comput 16: 1367-1372.

Matsumura Y, Yamashita T, Sasaki A, Nakata E, Kohno K, Masuda T, et al. (2016). A novel P2X4 receptor-selective antagonist produces anti-allodynic effect in a mouse model of herpetic pain. Sci Rep 6: 32461.

Miklavc P, Mair N, Wittekindt OH, Haller T, Dietl P, Felder E, et al. (2011). Fusion-activated Ca2+ entry via vesicular P2X4 receptors promotes fusion pore opening and exocytotic content release in pneumocytes. Proc Natl Acad Sci U S A 108: 14503-14508.

Miteva MA, Guyon F, & Tuffery P (2010). Frog2: Efficient 3D conformation ensemble generator for small compounds. Nucleic Acids Res 38: W622-627.

Richards D, Gever JR, Ford AP, & Fountain SJ (2019). Action of MK-7264 (gefapixant) at human P2X3 and P2X2/3 receptors and in vivo efficacy in models of sensitisation. Br J Pharmacol 176: 2279-2291.

Roe DR, & Cheatham TE, 3rd (2013). PTRAJ and CPPTRAJ: Software for Processing and Analysis of Molecular Dynamics Trajectory Data. J Chem Theory Comput 9: 3084-3095.

Sali A, & Blundell TL (1993). Comparative protein modelling by satisfaction of spatial restraints. J Mol Biol 234: 779-815.

Smith JA, Kitt MM, Butera P, Smith SA, Li Y, Xu ZJ, et al. (2020). Gefapixant in two randomised dose-escalation studies in chronic cough. Eur Respir J 55.

Stavrou A, Dayl S, & Schmid R (2020). Homology Modeling of P2X Receptors. Methods Mol Biol 2041: 65-75.

Stokes L, Layhadi JA, Bibic L, Dhuna K, & Fountain SJ (2017). P2X4 Receptor Function in the Nervous System and Current Breakthroughs in Pharmacology. Front Pharmacol 8: 291.

Tsuda M, Shigemoto-Mogami Y, Koizumi S, Mizokoshi A, Kohsaka S, Salter MW, et al. (2003). P2X4 receptors induced in spinal microglia gate tactile allodynia after nerve injury. Nature 424: 778-783.

Williams WA, Linley JE, Jones CA, Shibata Y, Snijder A, Button J, et al. (2019). Antibodies binding the head domain of P2X4 inhibit channel function and reverse neuropathic pain. Pain 160: 1989-2003.

Yamamoto K, Sokabe T, Matsumoto T, Yoshimura K, Shibata M, Ohura N, et al. (2006). Impaired flow-dependent control of vascular tone and remodeling in P2X4-deficient mice. Nat Med 12: 133-137.

Yang T, Shen JB, Yang R, Redden J, Dodge-Kafka K, Grady J, et al. (2014). Novel protective role of endogenous cardiac myocyte P2X4 receptors in heart failure. Circ Heart Fail 7: 510-518.

Figure Legends

Figure 1. 5-BDBD displays an allosteric mode of action (**A**) ATP-evoked Ca^{2+} responses from 1321N1 astrocytoma cells stably expressing human P2X2 (open circles) or P2X4 (closed circles; N=6). (**B**) 5-BDBD inhibition (30 minute incubation) of P2X4 (closed circles) but not P2X2 receptors (open circles; N=8). Both receptors activated with 1μM ATP (**C**) Effect of varying 5-BDBD concentrations (30 minute incubation) on ATP concentration-response relationship in 1321N1 astrocytoma cells stably expressing P2X4 (*N*=6). (**D**) Sequential mutation of 10 amino acid stretches in the ectodomain of P2X4 to the equivalent residues in P2X2 identified a region between residues 81-90 important for 5-BDBD activity. Substitutions between 71-80, 101-110, 131-140, 201-210, 221-220, 261-270, 281-290 and 291-300 produced non-functional chimeras (*N*=5). (**E**) Homology model of P2X4 in the ATP-bound (beige) open state based on zebrafish P2X4 (PDB:4DW1). Residues 81-90 can be located towards the top of the body region (red) and extended towards the orthosteric site (blue).

Figure 2. Molecular modelling identified an allosteric binding site for 5-BDBD (**A**) Representative 5-BDBD docking pose from molecular dynamics simulations. Relevant residues are shown as sticks, potential hydrogen bonding is indicated by dashes. (**B**) Carbonyl-guanidine distances between 5-BDBD and R301 (blue) and R82 (red), respectively for a representative molecular dynamics simulation. (**C**) Amide-carboxylate oxygen distances between 5-BDBD and E307. Blue and red represent the two carboxylate oxygens. (**D**) Distance between the Y300 hydroxyl group oxygen and the amide-NH (red) and carbonyl oxygen (blue). (**E**) Presence of hydrophobic interactions between 5-BDBD and relevant residues. For comparison residues are colour coded as in Figure 3B.

Figure 3. Site-directed mutagenesis of the allosteric site identified F81, M109, F178, Y300, R301 and I312 as important residues for 5-BDBD inhibition (**A**) Alignment of amino acids predicted to interact with 5-BDBD in the binding site between P2X1-7 (P2X4 numbering). Blue and orange depict which subunit the amino acid residues are located on. (**B**) Inhibitory activity of 5-BDBD against mutant P2X4 receptors. (**C**) A representative image of 5-BDBD binding to the wild-type P2X4 receptor. Residues implicated in 5-BDBD (purple) binding are highlighted in red (*N*=5 or 6 depending upon the mutation). (**D**) Representative images of 5-BDBD binding to the mutant receptors M109H, F178L, Y300A, R301K and I312G. The mutated residue is labelled and the distances between the amino acids and potential interactions with 5-BDBD are shown by dashes. Images were generated using Chimera.

Figure 4. 5-BDBD analogues identified key structural interactions between 5-BDBD and P2X4 (**A**) The structure of 5-BDBD and the positions of the halogen substitutions at R1, R2 and R3. Unmodified 5-BDBD has a bromine at position R2. (**B and C**) The IC_{50} values (**B**) and inhibitory activity (**C**) of the 5-BDBD analogues towards P2X4 stably expressed in 1321N1 astrocytoma cells (600 μM ATP and 30 μM 5-BDBD analogue were used to quantify inhibitory activity; *N*=3 independent experiments). (**D**) The distance between the carbonyl group of 5-BDBD/5-BDBD analogues and R301 in the binding pocket as determined through docking studies. (**E**) The penetration distance of 5-BDBD/5-BDBD analogues into the predicted binding site relative to the opening of the pocket as determined by docking studies. Images were generated using Chimera.

Figure 5. Constriction of the P2X4 allosteric binding site in the open-state may prevent the activity of 5-BDBD (**A**) Representative image depicting the predicted constriction of the 5-BDBD binding pocket and conformational changes between P2X4 in the closed (blue) and open (red) states. (**B**) The relative distance between amino acids T76, S77, L79, R82 and W84 on one subunit with the atoms CD1 or CD2 of L107 on the other subunit, in the closed and open channel. (**C**) Representative electrophysiology trace of a cell stimulated with 30 μM

ATP in the absence of 5-BDBD (black) or following a 3-minute pre-incubation with 20 μM 5-BDBD (red). (**D**) Representative electrophysiology trace of cells stimulated with 30 μM ATP for 2 seconds prior to the addition of 30 μM ATP and 20 μM 5-BDBD (red), or ATP and DMSO (black), during the desensitisation stage for 5 seconds. (**E**) Representative electrophysiology trace of cells stimulated with 30 μM ATP for 2 seconds prior to the addition of 30 μM ATP and 10 μM BX-430 (red), or ATP and DMSO (black), during the desensitisation stage for 5 seconds. (**F**) The time constant values for current decay (Tau) for the desensitisation stage in the presence of DMSO, 5-BDBD or BX-430. Traces and data are representative of 17, 7 and 5 cells for the vehicle control, 5-BDBD, and BX-430, respectively. *$p<0.05$ *vs* vehicle, **$p<0.05$ *vs* 5-BDBD. Images were generated using Chimera.
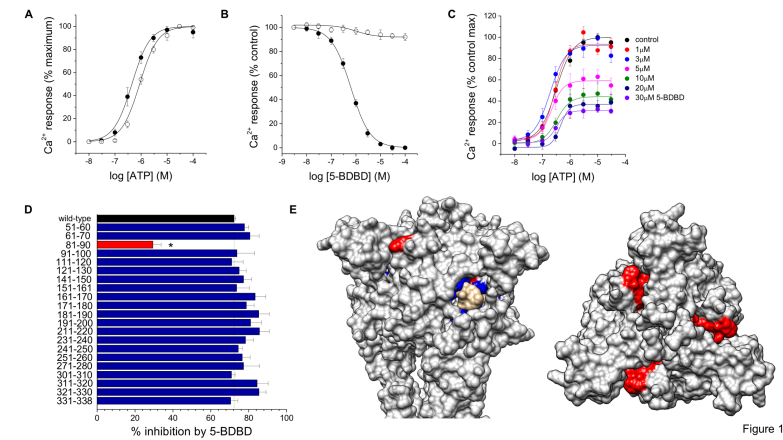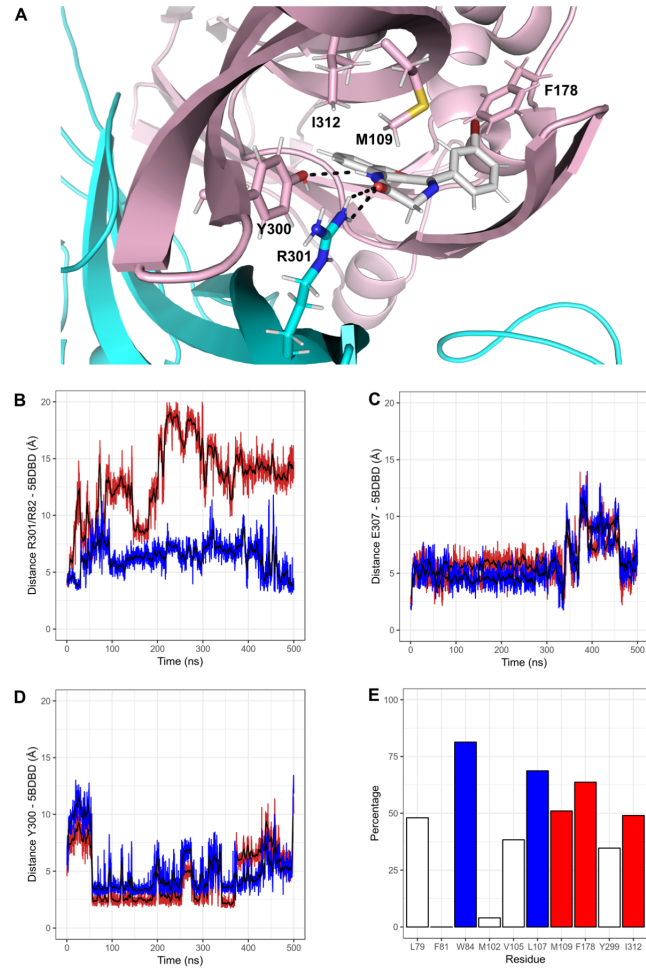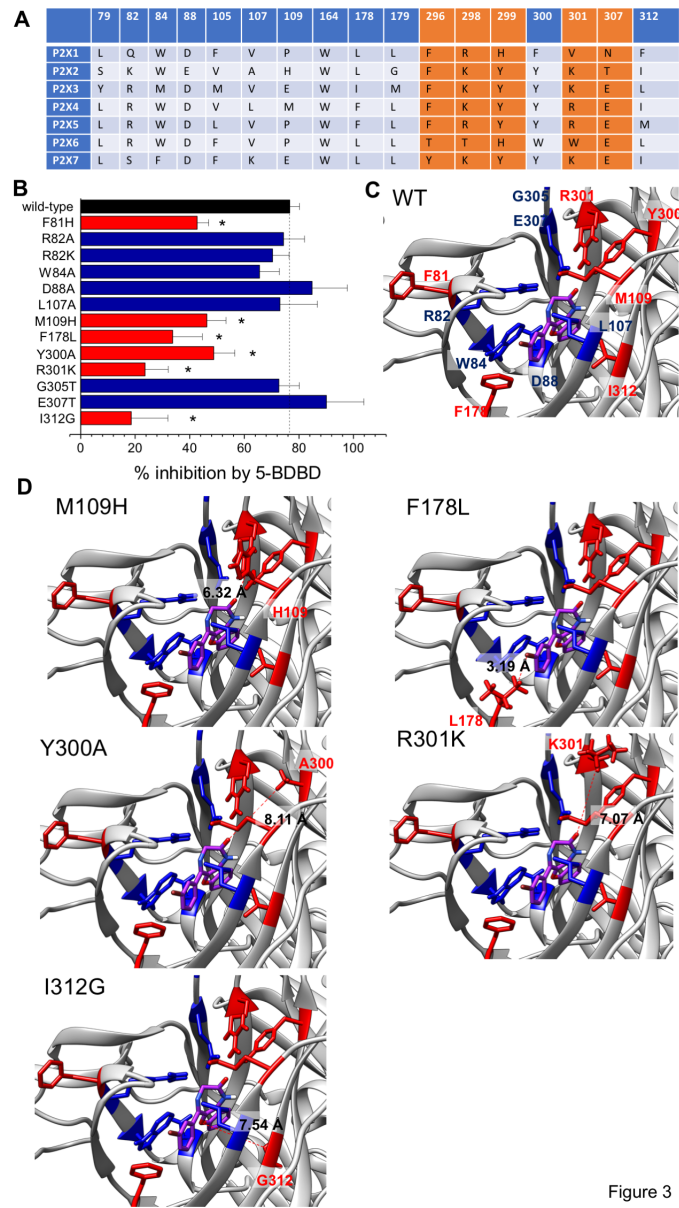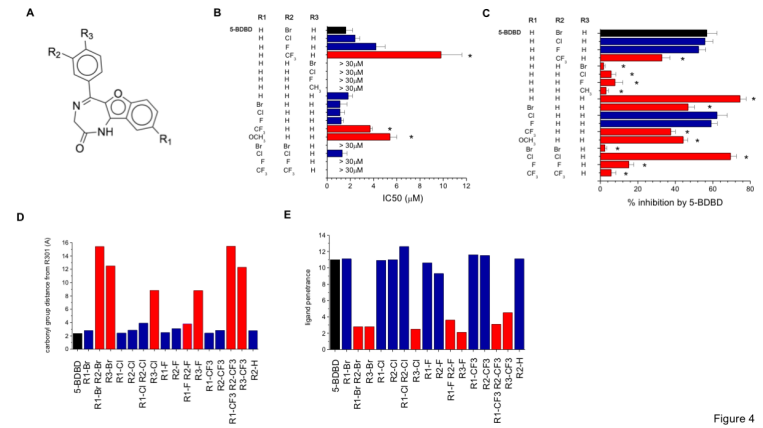

Figure 1

Figure 2

Figure 3

Figure 4

Figure 5